Journal of the Korean Astronomical Society
51: 155 ∼ 164, 2018 October

http://dx.doi.org/10.5303/JKAS.2018.51.5.155
pISSN: 1225-4614 · eISSN: 2288-890X
http://jkas.kas.org

Infrared Two-Color Diagrams of AGB Stars and Planetary Nebulae Using WISE Data

Kyung-Won Suh

Department of Astronomy and Space Science, Chungbuk National University, 1 Chungdae-ro, Seowon-Gu, Cheongju 28644, Korea; kwsuh@chungbuk.ac.kr

Received August 7, 2018; accepted October 11, 2018

Abstract: We present various infrared two-color diagrams (2CDs) using WISE data for asymptotic giant branch (AGB) stars and Planetary Nebulae (PNe) and investigate possible evolutionary tracks. We use the sample of 5036 AGB stars, 660 post-AGB stars, and 2748 PNe in our Galaxy. For each object, we cross-identify the IRAS, AKARI, WISE, and 2MASS counterparts. To investigate the spectral evolution from AGB stars to PNe, we compare the theoretical model tracks of AGB stars and post-AGB stars with the observations on the IR 2CDs. We find that the theoretical dust shell model tracks can roughly explain the observations of AGB stars, post-AGB stars, and PNe on the various IR 2CDs. WISE data are useful in studying the evolution of AGB stars and PNe, especially for dim objects. We find that most observed color indices generally increase during the evolution from AGB stars to PNe. We also find that $Fe_{0.9}Mg_{0.1}O$ dust is useful to fit the observed WISE W3-W4 colors for O-rich AGB stars with thin dust shells.

Key words: stars: AGB and post-AGB — dust, extinction — circumstellar matter — infrared: stars — radiative transfer

1. Introduction

Asymptotic giant branch (AGB) stars are generally believed to be in the last evolutionary phases for low mass stars (M $\leq$ 10 $M_{\odot}$) evolving rapidly from the red giant branch into planetary nebulae (PNe). Most AGB stars are long-period variables with large amplitude pulsations which produce dusty stellar winds with high mass-loss rates ($10^{-8} - 10^{-4} M_{\odot}/yr$; e.g., Suh 2014).

Due to circumstellar amorphous silicate dust, low mass-loss rate O-rich AGB (LMOA) stars with thin dust envelopes show 10 μm and 18 μm emission features and high mass-loss rate O-rich AGB (HMOA) stars with thick dust envelopes show absorbing features at the same wavelengths (e.g., Suh 1999). The spectral energy distributions (SEDs) of LMOA stars suggest the presence of amorphous alumina (Al_2O_3; Suh 2016) and Fe-Mg oxides (Th. Posch et al. 2001) as well as silicate dust. The SEDs of HMOA stars can be reproduced by crystalline silicates and water ice as well as amorphous silicate (e.g., Suh & Kwon 2013). For C-rich AGB stars, featureless amorphous carbon (AMC) and SiC grains, which produce the 11.3 μm feature, can reproduce the SEDs (e.g., Suh 2000).

As the star leaves the AGB phase, its dust envelope gets thinner and the central core become hot enough ($\sim$ 30,000 K) to ionize its circumstellar material and become a planetary nebula (PN) (e.g., Kwok 2000). The hot core lights up the expanding envelope for about 10,000 years. At the end-point of stellar evolution, most stars between 1 and 10 $M_{\odot}$ would become PNe.

Corresponding author: K.-W. Suh

Post-AGB stars are in the intermediate phase between the end of the AGB phase and the beginning of the PN phase. The dust shell that formed in the AGB phase detaches from the central core and becomes optically thin during the post-AGB phase (e.g., Hrivnak et al. 1989). The time-scale of the post-AGB phase is believed to be rather short (within a thousand years; e.g., Suh 2015).

Suh (2015) presented infrared two-color diagrams (2CDs) for AGB stars, post-AGB stars, and PNe and investigated possible evolutionary tracks. In this paper, we present IR 2CDs for a larger sample of stars using new WISE data and investigate possible evolutionary tracks. We use theoretical dust shell models for AGB stars and post-AGB stars and compare the theory with the observations of AGB stars, post-AGB stars, and PNe on the various IR 2CDs.

2. Sample Stars

We use catalogs of AGB stars, post-AGB stars, and PNe from the available literature. Table 1 lists the reference, total number of objects, and numbers of the cross-identified Infrared Astronomical Satellite (IRAS) point source catalog (PSC), AKARI PSC, Two-Micron All-Sky Survey (2MASS), and Wide-field Infrared Survey Explorer (WISE) counterparts for each class.

2.1. Infrared Photometric Data

The IRAS PSC (Beichman et al. 1988) provided photometric data in four bands (12, 25, 60, and 100 μm). AKARI (Murakami et al. 2007) conducted an all-sky survey with the infrared camera (IRC) which provided PSC data in two bands (9 and 18 μm; Ishihara et al.

Table 1
Sample of AGB stars, post-AGB stars, and PNe

Class	Reference	Number	IRAS PSC	AKARI PSC	2MASS	WISE	W2 data[1]
O-AGB	Suh & Hong (2017)	3828	3828	3674	3828	3822	971 (2224)
C-AGB	Suh & Hong (2017)	1168	1168	1152	1168	1167	119 (350)
post-AGB	Szczerba et al. (2007)	326	236	254	326	324	241
PPNe	Kohoutek (2001)	334	325	300	333	333	236
PNe	Kohoutek (2001)	1510	927	890	1508	1509	1261
MPNe	MASH 1[2]	903	161	259	903	901	697
MPNe	MASH 2[3]	335	89	99	335	335	274

[1]Number of good quality data in the WISE W2 band (quality A). For AGB stars, the number in parenthesis denotes the number of quality A and B data. [2]Parker et al. (2006). [3]Miszalski et al. (2008).

2010) and far-infrared surveyor (FIS) which provided bright-source catalogue (BSC) data in four bands (65, 90, 140, and 160 μm; Yamamura et al. 2010). 2MASS (Cutri et al. 2003) provided fluxes in J (1.25 μm), H (1.65 μm), and K (2.17 μm) bands. The field of view (FOV) pixel sizes of the IRAS, AKARI PSC, AKARI BSC, and 2MASS images are 0.′75x(4.′5-4.′6), 10″, 30″, and 2″, respectively.

In 2010, the WISE (Wright et al. 2010) surveyed the entire sky in the 3.4 μm (W1), 4.6 μm (W2), 12 μm (W3), and 22 μm (W4) bands. For the four WISE bands, the FOV pixel sizes are 2.″75, 2.″75, 2.″75, and 5.″5, and the 5σ photometric sensitivities are 0.068, 0.098, 0.86, and 5.4 mJy. The WISE data would be useful, especially for studying dim objects.

2.2. Counterparts for IRAS PSC sources

Because IRAS has very low angular resolution, the 2MASS or WISE counterpart obtained from the IRAS PSC position can, in fact, be a different object. The 2MASS or WISE counterpart obtained from the AKARI data (with a higher angular resolution; see Section 2.1) would be much more reliable.

When the position is known only from the IRAS PSC, we cross-identify the AKARI PSC or BSC counterpart by finding the nearest source within 60″ using the position given in the IRAS PSC (version 2.1). We cross-identify 2MASS and WISE counterparts using the position of the available AKARI PSC or BSC counterpart. Only when there is no AKARI counterpart, we use the position of the IRAS PSC.

2.3. AGB stars

A catalog of AGB stars for 3003 O-rich, 1168 C-rich objects in our Galaxy was presented by Suh & Kwon (2011). Suh & Hong (2017) presented a revised list of 3828 O-rich and 1168 C-rich AGB stars based on the IRAS PSC. We find the AKARI PSC, 2MASS, and WISE counterparts as described in Section 2.2.

Because a major portion of Galactic AGB stars are bright objects which may saturate the WISE detectors, these data would be useful only for a portion of Galactic AGB stars. In the WISE W2 band, good quality (quality A) data are available only for 25% (or 10%) of O-rich (or C-rich) AGB stars which is a much smaller portion compared with other classes (see Table 1). Only for AGB stars, we need to use more data (quality A and B) in the WISE W2, W3, and W4 bands for plotting meaningful 2CDs (see Section 3).

It is possible that some sample stars are contaminated by other sources (e.g., star forming regions or young stellar objects). Therefore, comparison between the fluxes from different catalogs would be useful to verify the cross-identification. Figure 1 shows the comparison of IRAS PSC and WISE fluxes for the sample AGB stars (see Table 1). For the IRAS PSC, we use only good quality (quality 3) data. For the WISE, we use only quality A and B data. The least-square fit line and parameters are also shown for O-rich and C-rich AGB stars. The overall comparison is fairly consistent for most objects. Some objects show large deviations (the IRAS flux is much larger than the WISE flux) possibly due to the contamination. Because the FOV of the IRAS is much larger, the IRAS flux can be larger when the contamination from nearby other sources occurs.

2.4. Post-AGB stars

The intermediate phase between the end of the AGB phase and the PN phase is now called the post-AGB phase, which was also called the proto-PN or pre-PN phase (e.g., Hrivnak et al. 1989; Kwok 2000; Kohoutek 2001; Szczerba et al. 2007).

For post-AGB stars, we use the 326 objects from the catalog of post-AGB stars by Szczerba et al. (2007) and use the IRAS PSC and 2MASS counterparts listed in Szczerba et al. (2007). We cross-identify the AKARI and WISE counterparts by finding the nearest source within 30″ using the position given in Szczerba et al. (2007) for each object.

Kohoutek (2001) presented a list of 334 pre-PNe (PPNe) from the catalogue of Galactic Planetary Nebulae. For PPNe, we use position of the IRAS PSC counterparts for 325 objects given in Kohoutek (2001) to find AKARI PSC, 2MASS, and WISE as described in Section 2.2. For other 9 objects, we find the counterpart by finding the nearest source within 60″ using the position given in Kohoutek (2001).

2.5. Planetary Nebulae

We use the catalogue of Galactic Planetary Nebulae (Updated Version 2000; Kohoutek 2001 which contains

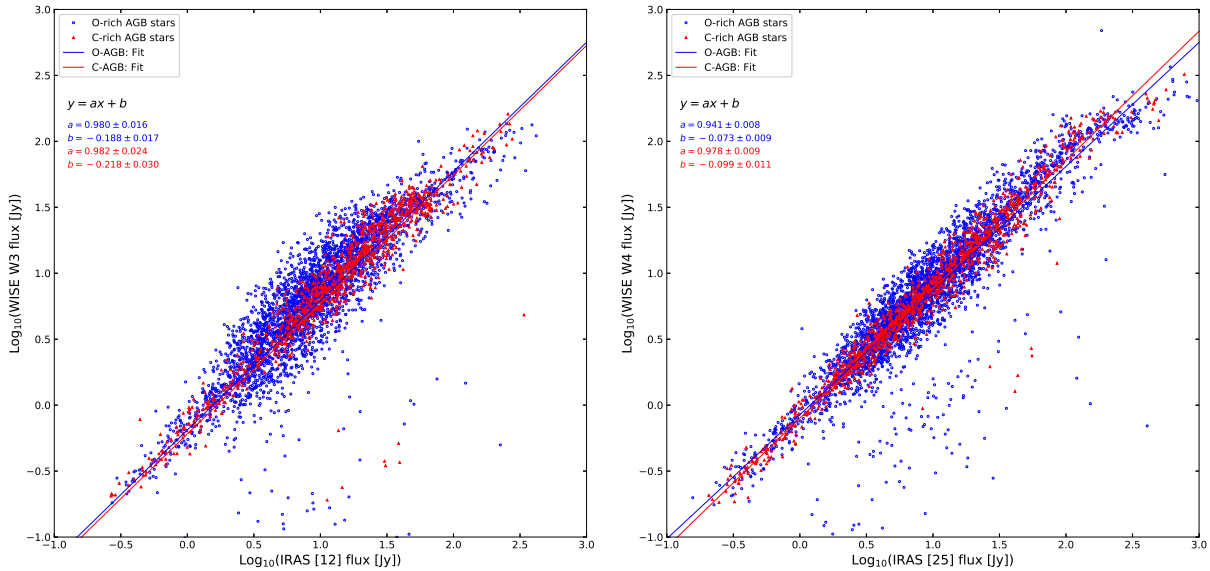

Figure 1. Comparison of IRAS PSC and WISE fluxes for AGB stars (see Table 1). The least-square fit line and parameters are also shown for O-rich and C-rich AGB stars.

1510 objects classified as galactic PNe. For the position, we use the more accurate position data presented by Kerber et al. (2003) for the 1312 PNe to cross-identify the AKARI, 2MASS, and WISE counterparts by finding the nearest source within 30″. For others, we use IRAS PSC position or the position information listed in Kohoutek (2001) to cross-identify the AKARI, 2MASS and WISE counterparts.

The Macquarie/AAO/Strasbourg Hα (MASH) 1 and 2 catalogs (Parker et al. 2006; Miszalski et al. 2008) listed 1238 new Galactic PNe. The MASH PNe (hereafter MPNe) are typically dimmer and of lower surface brightness than those found in most previous surveys. Typical MPNe are believed to be more evolved PNe with very thin outer envelopes. We cross-identify the IRAS, AKARI, 2MASS, and WISE counterparts by finding the nearest source within 30″ (60″ for the IRAS) using the position given in the MASH catalogs (Parker et al. 2006; Miszalski et al. 2008).

3. Infrared Two-Color Diagrams

Only for a relatively small number of stars, we have complete or nearly complete SEDs from infrared spectroscopy. A large number of stars have infrared photometric fluxes from the near infrared to the far infrared band thanks to the IRAS, AKARI, 2MASS, and WISE observations. Although the photometric fluxes are less useful than a full SED, the large number of observations in various wavelength bands can be used to form 2CDs, which can be compared to theoretical models. IR 2CDs are useful to statistically distinguish AGB stars, post-AGB stars, and PNe (e.g., Suh 2015). We may use IR 2CDs to find new candidate objects for AGB stars (e.g., Suh & Hong 2017).

Figures 2 and 3 show the IR 2CDs for the sample stars (see Section 2). For these stars, we obtain photometric data in three bands (12, 25, and 60 μm) of the IRAS PSC, 2MASS data in K (2.17 μm) band, and WISE data in three bands (W2, W3, and W4). Generally, the stars that have thick dust shells with large optical depths are located in the upper-right region of the 2CDs. On all of the 2CDs, we also plot theoretical model tracks for AGB stars and post-AGB stars (see Section 4).

The color index is defined by

$$M_{\lambda 1} - M_{\lambda 2} = 2.5 \log_{10} \frac{F_{\lambda 2}/ZMC_{\lambda 2}}{F_{\lambda 1}/ZMC_{\lambda 1}} \qquad (1)$$

where $ZMC_{\lambda i}$ is the zero magnitude calibration at given wavelength (λi) (e.g., Suh & Kwon 2011).

In plotting the IR 2CDs, we use only those objects with good quality (quality 3 for IRAS; quality A for 2MASS and WISE) observational data in all wavelength bands. Only for AGB stars, we use more data (quality A and B) in the WISE bands for the reason described in Section 2.3.

The upper panel of Figure 2 plots an IRAS 2CD using [25]-[60] versus [12]-[25]. The lower panel of Figure 2 plots a WISE 2CD using W3-W4 versus W2-W3. The upper panel of Figure 3 plots an AKARI-IRAS 2CD using [9]-[12] versus [12]-[25]. The lower panel of Figure 3 plots a 2MASS-WISE 2CD using W3-W4 versus K-W3. We will discuss meanings of these 2CDs in Section 5.

Table 2 shows averaged observed colors of the sample stars for various IR colors used for this work. Figure 4 shows the error bar plots of the observed colors used for the four IR 2CDs presented in Figures 2 and 3.

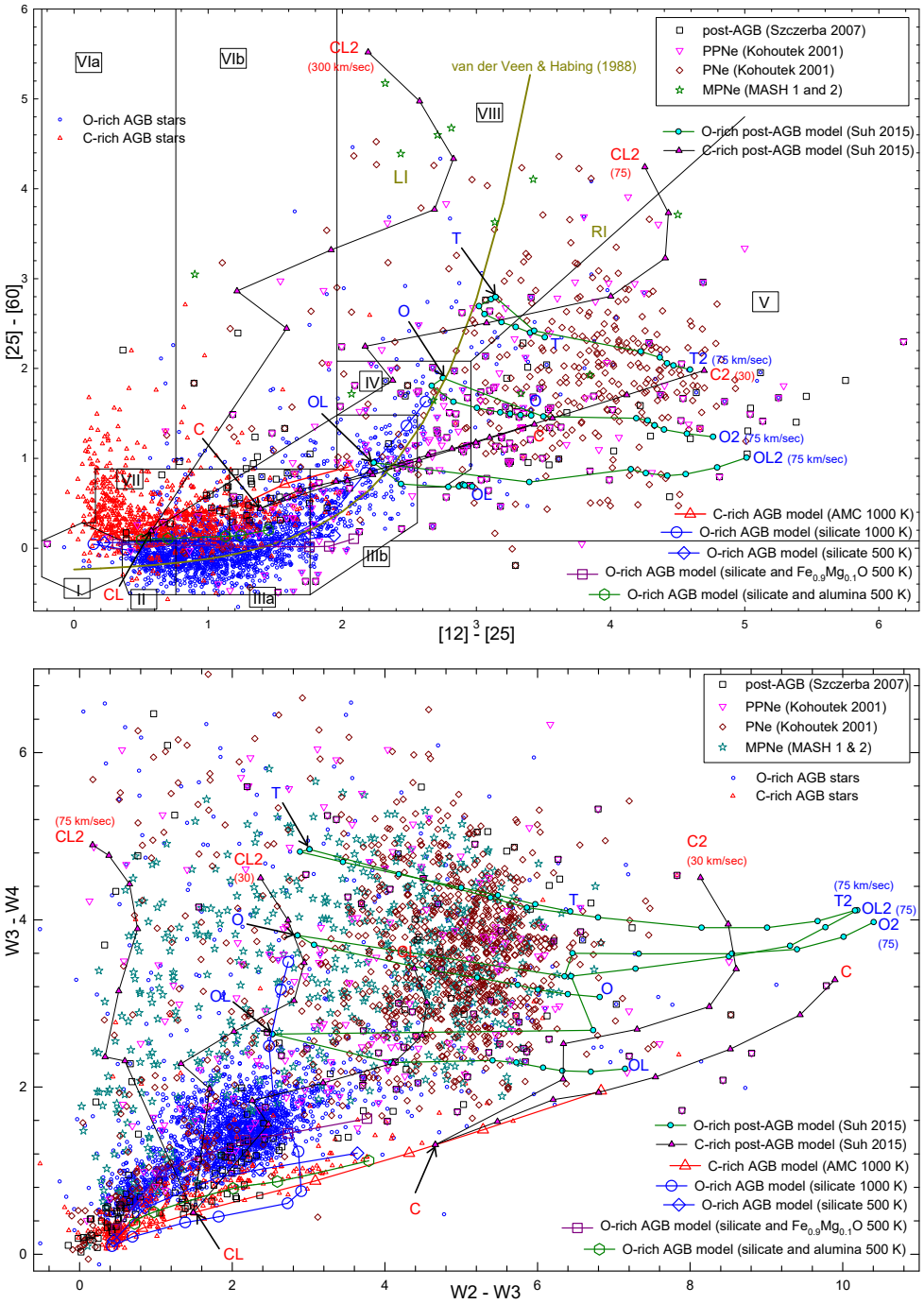

Figure 2. IR 2CDs for the sample stars (see Table 1). Theoretical dust shell model tracks are also shown (see Section 4). For C-rich AGB models (T_c = 1000 K): τ_{10} = 0.01, 0.1, 1, 2, 3, 5, and 7 from left to right. For O-rich AGB models (T_c = 1000 K): τ_{10} = 0.005, 0.01, 0.05, 0.1, 0.5, 1, 3, 7, 15, 30, and 40 from left to right. For O-rich AGB models (T_c = 500 K): τ_{10} = 0.005, 0.01, 0.05, 0.1, and 0.5 from left to right. The start points of the post-AGB model tracks are indicated by black arrows.

4. THEORETICAL DUST SHELL MODELS

On all of the 2CDs in Figures 2 and 3, theoretical model tracks for AGB stars and post-AGB stars are plotted to be compared with the observations. We use spherically symmetric dust shell models for AGB stars and post-AGB stars.

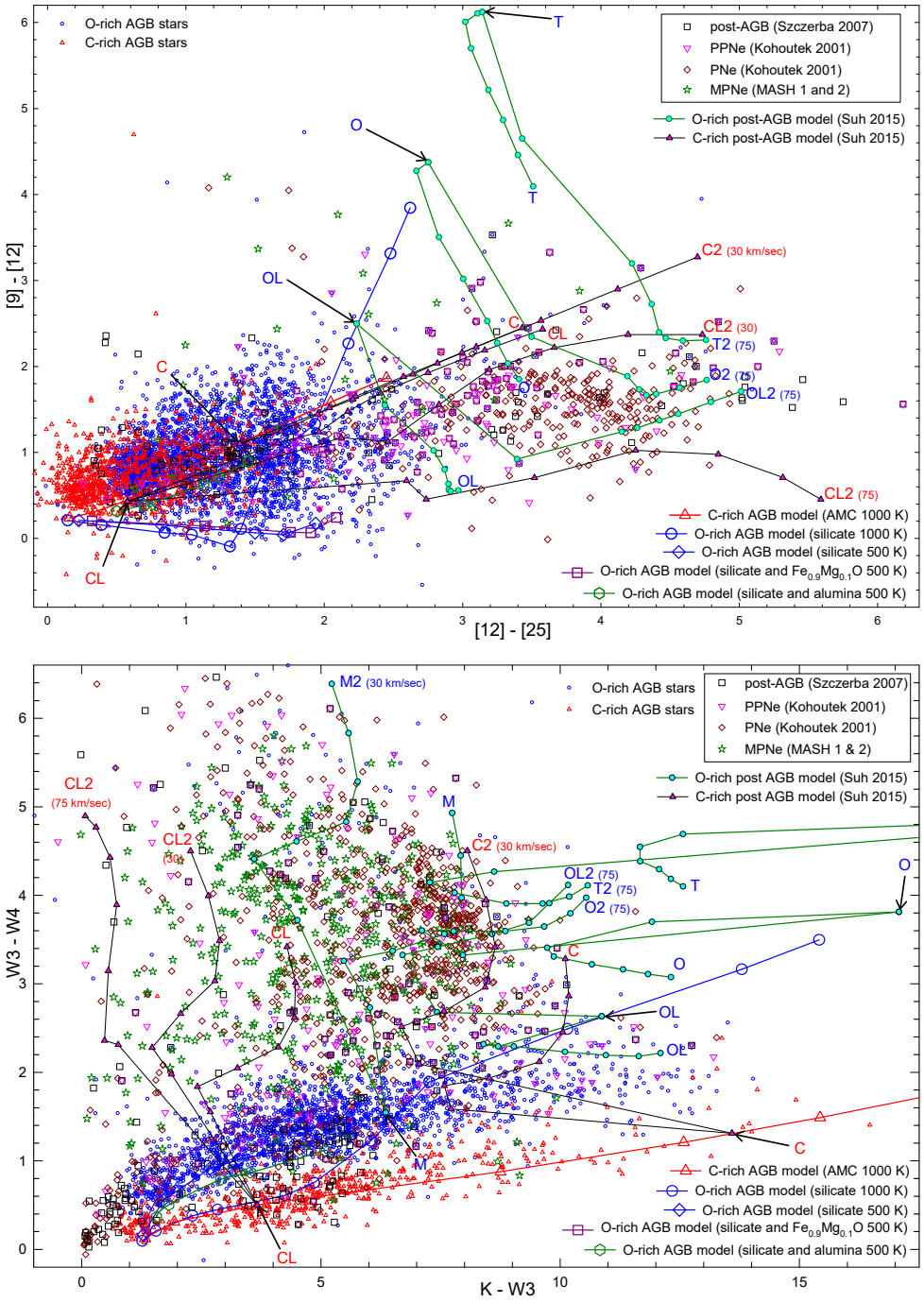

Figure 3. IR 2CDs for the sample stars (see Table 1). Theoretical dust shell model tracks are also shown (see Section 4). For C-rich AGB models (T_c = 1000 K): τ_{10} = 0.01, 0.1, 1, 2, 3, 5, and 7 from left to right. For O-rich AGB models (T_c = 1000 K): τ_{10} = 0.005, 0.01, 0.05, 0.1, 0.5, 1, 3, 7, 15, 30, and 40 from left to right. For O-rich AGB models (T_c = 500 K): τ_{10} = 0.005, 0.01, 0.05, 0.1, and 0.5 from left to right. The start points of the post-AGB model tracks are indicated by black arrows.

4.1. Dust Shell Models for AGB Stars

For AGB stars, we use the radiative transfer code DUSTY (Ivezić & Elitzur 1997) for a spherically symmetric dust shell. We use a continuous ($\rho \propto r^{-2}$) dust density distribution and the dust formation temperature (T_c) of 1000 K or 500 K. The inner radius of the dust shell is set by T_c and the outer radius of the dust

Table 2
Averaged observed colors of the sample stars

Class[1]	[12]-[25]	[25]-[60]	W2-W3	W3-W4	K-W3	[9]-[12]
O-AGB	1.34±0.63 (3568)	0.276±0.66 (2099)	2.04±1.1 (2186)	1.39±0.86 (3478)	5.06±2.6 (2209)	0.984±0.47 (3157)
C-AGB	0.653±0.49 (1098)	0.403±0.36(768)	1.49±1.4 (342)	0.634±0.49 (1011)	4.83±2.8 (635)	0.741±0.36 (1051)
post-AGB	2.51±1.3 (192)	1.22±0.73 (180)	2.67±2.3 (209)	2.14±1.6 (224)	3.79±2.8 (245)	1.35±0.63 (195)
PPNe	2.77±1.0 (225)	1.41±0.94 (226)	3.72±2.0 (214)	3.08±1.4 (247)	5.75±2.7 (204)	1.45±0.60 (161)
PNe	3.37±0.99 (370)	2.23±0.87 (653)	4.12±1.7 (1104)	3.37±1.2 (1152)	5.60±2.4 (826)	1.48±0.51 (314)
MPNe[2]	2.06±1.0 (40)	2.92±1.1 (63)	3.09±1.8 (634)	3.48±1.0 (669)	4.56±2.0 (539)	1.96±1.5 (32)

The number in parenthesis denotes the number of the good quality observed color data used for this work. [1]See Table 1 for references. [2]MASH 1 and 2 objects which consist of three types (867 True, 206 Likely, and 165 Possible).

shell is taken to be 10^4 times the inner radius. The radii of spherical dust grains are assumed to be 0.1 μm uniformly. We use 10 μm as the fiducial wavelength of the dust optical depth (τ_{10}). For the central star, we assume that the luminosity is 10^4 $L_{\odot}$.

For O-rich AGB stars, we use optical constants of warm and cold silicate dust from Suh (1999). We compute eleven models (τ_{10} = 0.005, 0.01, 0.05, 0.1, 0.5, 1, 3, 7, 15, 30, and 40). We use warm silicate for LMOA stars (7 models with $\tau_{10} \leq 3$) and cold silicate for HMOA stars (4 models $\tau_{10} > 3$). We assume that the stellar blackbody temperature is 2500 K for $\tau_{10} \leq 3$ and 2000 K for $\tau_{10} > 3$.

For LMOA stars with thin dust shells, Suh (2004) pointed out that a lower T_c ($500 \leq T_c < 1000$ K) is required. Also alumina and Fe-Mg oxide grains as well as silicates are necessary to reproduce the observed SEDs (see Section 1).

For the LMOA stars with thin dust shells (five models: τ_{10} = 0.005, 0.01, 0.05, 0.1, 0.5), we also use T_c of 500 K. Also, we use three different dust opacity models: a simple mixture of warm silicate and $Fe_{0.9}Mg_{0.1}O$ (20% by number) and a simple mixture of warm silicate and alumina (20% by number) as well as pure warm silicate. For $Fe_{0.9}Mg_{0.1}O$ dust, we use the optical constants from Henning et al. (1995). For alumina dust, we use the optical constants from Suh (2016) which are derived from the optical constants in narrower wavelength range obtained by Begemann et al. (1997).

For C-rich AGB stars, we use optical constants of amorphous carbon (AMC) dust from Suh (2000). We compute seven models (τ_{10} = 0.01, 0.1, 1, 2, 3, 5, and 7). We assume that the stellar blackbody temperature is 2300 K for $\tau_{10} \leq 0.1$ and 2000 K for $\tau_{10} > 0.1$.

4.2. Dust Shell Models for Post-AGB Stars

To find the spectral evolution of post-AGB stars, Suh (2015) used various dust shell models with different mass-loss rates for each core-mass model of the central star. The author presented radiative transfer model results for detached dust shells around evolving central stars in the post-AGB phase.

For this work, we use the post-AGB models of Suh (2015) adapted for the new IR 2CDs. For the low core-mass model, we use one base model (M) for low-mass O-rich post-AGB stars and two models (CL and C) for C-rich post-AGB stars (see Table 3 in Suh 2015). For the high core-mass model, we use three models (OL, O, and T) for high-mass O-rich post-AGB stars (see Table 4 in Suh 2015). For all dust shell models, the expansion velocity (v_{exp}) and mass-loss rate ($\dot{M}$) of the dust shell remain constant during the whole post-AGB phase. We assume that v_{exp} = 15 km s^{-1} for all base models (e.g., C; OL) and $v_{exp} > 15$ km s^{-1} for all derived models (e.g., C2; OL2).

We plot the theoretical model tracks for post-AGB stars (see Tables 3 and 4 in Suh 2015 for detailed model parameters) on the 2CDs in Figures 2 and 3. On the 2CDs, the tip of an arrow indicates the point at the start of the post-AGB phase for each post-AGB model track. At the end point of the each model track, the base or derived model name is labeled.

5. COMPARISON BETWEEN THEORY AND OBSERVATIONS

On various IR 2CDs in Figures 2 and 3, we compare the observations with the theoretical dust shell models for AGB stars and post-AGB stars. Similar work was done by Suh (2015). In this work, we use new WISE data as well as IRAS and 2MASS data for more sample stars (AGB stars and MPNe).

For all of the observed colors ([12]-[25], [25]-[60], W2-W3, W3-W4, K-W3, and [9]-[12]), the averaged color of AGB stars is bluer than that of PNe (see Table 2 and Figure 4). Note that this difference is systematic except for the K-W3 color, for which the error bars overlap. The main reason for this difference would be that detached dust shells generally produce redder colors during the post-AGB phase (see the post-AGB model tracks on the 2CDs in Figures 2 and 3).

5.1. Limitations of the Theoretical Models

The simple theoretical dust shell models used in this work (see Section 4) can reproduce the observed SEDs reasonably well for most AGB stars and some post-AGB stars, especially for the objects with thick dust shells (e.g., Kwok 2000; Suh 2004). However, because the theoretical models do not consider gas-phase radiation processes, the models can not explain various emission features of typical PNe and post-AGB stars. Also, the spherically symmetric dust shell models do not consider some dust species (e.g., PAH) and non-spherical geometry.

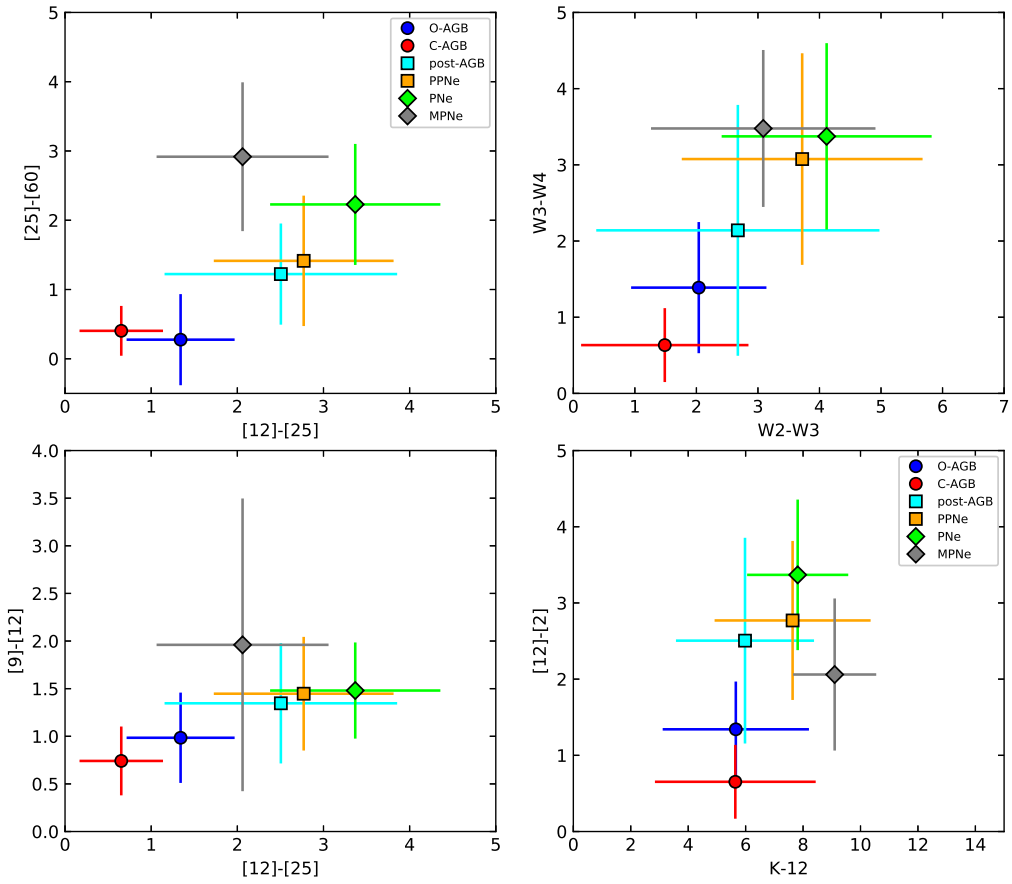

Figure 4. Averaged observed colors of the sample stars (see Table 2) used for 2CDs (see Figures 2 and 3).

Figure 5 shows relative response functions of IRAS (12 and 25 μm) and WISE W3 and W4 (12 and 22 μm) bands. The wavelength of the $Fe_{0.9}Mg_{0.1}O$ dust feature, which is considered in the theoretical model for LMOA stars with thin dust shells (see Section 4.1), is indicated. The fine emission features due to gas-phase ions and PAH for typical PNe (from Gutenkunst et al. 2008), which are not considered by the theoretical models in this work, are also indicated. The difference in the response functions could affect the efficiency in detecting the emission features in the wavelength range.

5.2. [25]-[60] versus [12]-[25]

The upper panel of Figure 2 plots an IRAS 2CD using [25]-[60] versus [12]-[25]. Since van der Veen & Habing (1988) divided the 2CD into eight regions, this has been widely used for studying various heavenly bodies. Though the number of available data for dim objects (e.g., MPNe) is small, the boundaries among different classes (AGB stars, post-AGB stars, and PNe) look clearer than any other 2CDs.

On this 2CD, the effects of $Fe_{0.9}Mg_{0.1}O$ and alumina dust on the model colors are rather minor compared with other 2CDs (see next subsections).

As noted by Suh (2015), the brown line which is the evolutionary tracks for late-type stars suggested by van der Veen & Habing (1988) roughly matches with the model tracks of AGB stars and the start points of the post-AGB model tracks. Centering around the brown line, the right and left regions (RI and LI) are indicated. As discussed by Suh (2015), the end points of all theoretical dust shell models with moderate expansion velocity (v_{exp}) converges to RI as well as the most of the observed PNe.

On the other hand, the objects in LI are likely to be precursors of bipolar PNe or binary systems (e.g., Sevenster 2002), to which the post-AGB dust shell models may not be applicable. Because end points of some low core-mass post-AGB model tracks with large v_{exp} are located in LI, it could be possible that some single stars with thin spherical dust shells may also evolve to LI.

Furthermore, we find that most MPNe are also located in LI. MPNe have a systematically smaller averaged [12]-[25] colors index than normal PNe (see Table 2 and Figure 4). Compared with normal PNe, old PNe would have thinner and more detached dust shell, which would produce bluer [12]-[25] and redder [25]-[60] colors. If MPNe are really older PNe, they would be located in the upper-left region on the 2CD. Observed [12]-[25] colors show this evolution, but the error bars

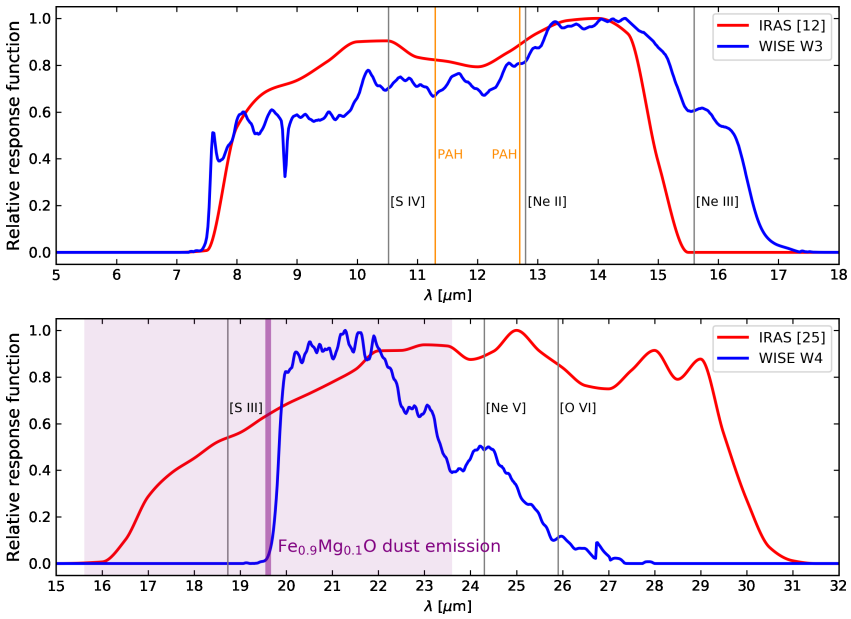

Figure 5. Relative response functions for IRAS and WISE bands. The wavelengths of the broad $Fe_{0.9}Mg_{0.1}O$ dust emission feature for AGB stars and fine gas-phase and PAH emission features for typical PNe are also indicated. For the dust feature, the representative line width (FWHM for a sphere with radius 0.1 μm) is indicated by the purple shaded area.

for [25]-[60] colors overlap (see Figure 4).

5.3. W3-W4 versus W2-W3

The lower panel of Figure 2 plots a WISE 2CD using W3-W4 versus W2-W3. Compared with the IRAS 2CD, the number of available MPNe objects are much larger.

For O-rich AGB stars with thin dust shells, it is not possible to fit the observations using only silicate dust. We find that $Fe_{0.9}Mg_{0.1}O$ dust (20% abundance) is useful to fit W3-W4 colors. When we vary the abundance of $Fe_{0.9}Mg_{0.1}O$ dust from 10% to 40%, the model covers much wider region on the 2CD where most of observed points are populated. On the other hand, the effect of $Fe_{0.9}Mg_{0.1}O$ dust on the IRAS [12]-[25] is much smaller (see Section 5.2). This is could be because the WISE W4 band is more sensitive to $Fe_{0.9}Mg_{0.1}O$ dust (see Section 5.6).

Compared with normal PNe, MPNe show bluer [12]-[25] possibly because older PNe have thinner and more detached dust shells (see Section 5.2). Because the W3-W4 color is similar to the [12]-[25] color, we may expect that MPNe would show bluer W3-W4 colors than normal PNe if MPNe are really older PNe. But we cannot find this effect on this 2CD and error bars overlap. This could be because some gas-phase emission lines affect the IRAS and WISE fluxes differently (see Figure 5). Or it is possible that a major portion of MPNe are not really more evolved PNe, they could be just more distant ones.

Figure 6 shows the error bar plots of the observed WISE colors for PNe and MPNe. For MPNe, the colors for three different types (true, likely, and possible) are compared. If possible MPNe are really older than likely PNe and likely PNe are really older than true PNe, the colors would change during the evolution into more evolved PNe (PNe, true MPNe, likely MPNe, and possible MPNe). We cannot find any color evolution from Figure 6 because all error bars overlap.

5.4. [9]-[12] versus [12]-[25]

The upper panel of Figure 3 plots an IRAS-WISE 2CD using [9]-[12] versus [12]-[25]. For the O-rich AGB model (T_c = 1000 K), the model [9]-[12] color initially gets bluer as the 10 μm silicate emission feature becomes more prominent, then it gets redder when the 10 μm silicate feature changes from emission to absorption.

As noted by Suh & Kwon (2011), alumina dust is useful to fit the AKARI [9]-[12] colors for AGB stars. Alumina dust produce larger [9]-[12] colors because the emission feature at 11.8 μm influence the shape of the SED at $\lambda \sim 10$ μm (see Section 5.6). On the other hand, the effects of $Fe_{0.9}Mg_{0.1}O$ dust on [9]-[12] and [12]-[25] colors are rather minor.

5.5. W3-W4 versus K-W3

The lower panel of Figure 3 plots a 2MASS-WISE 2CD using W3-W4 versus K-W3. On this 2CD, O-rich and C-rich AGB stars are divided more clearly because silicate produces larger W3-W4 for given K-W3 than AMC. There is a similar effect in an IRAS-2MASS 2CD using [12]-[25] versus K-[12] (e.g., Suh & Kwon 2011; Suh 2015). Again, $Fe_{0.9}Mg_{0.1}O$ dust is very useful to fit W3-W4 colors for LMOA stars with thin dust shells.

K-W3 post-AGB model colors are generally much redder than the observed colors of PNe. This could be

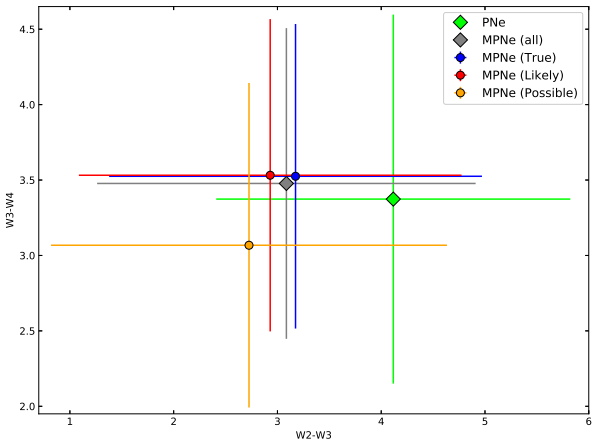

Figure 6. Averaged observed WISE colors for PNe and MPNe (see Table 2). For MPNe, the colors for three different types (true, likely, and possible) are compared.

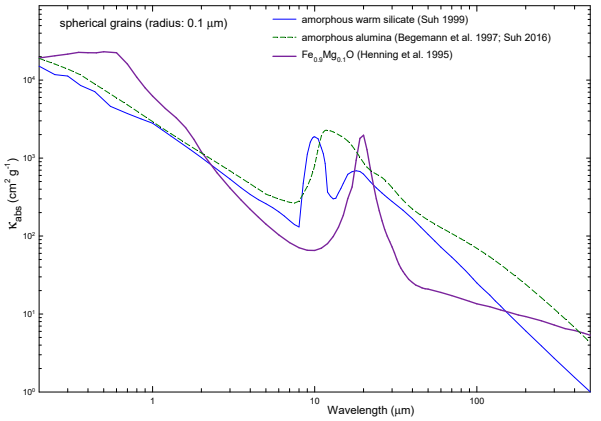

Figure 7. Dust opacity functions of warm silicate, alumina, and $Fe_{0.9}Mg_{0.1}O$. These three dust species are used for LMOA stars with thin dust shells (see Section 4.1).

because typical PNe and post-AGB stars show strong H_2 line emission in the 2MASS K band (e.g., Davis et al. 2003; Froebrich et al. 2011), which makes the observed K-W3 colors much bluer.

Non-spherical geometry could lead to scatter in values for the observed K-W3 colors. Though the theoretical models used in this work consider only spherically symmetric dust shells, the degree of occultation of the central star by a circumstellar disk or non-spherical envelope would have a strong impact on the measured K band magnitude as a function of viewing angle.

Unlike all other colors, the K-W3 color index does not show a systematic increase during the evolution from AGB stars to PNe (see Figure 4). Again, this could be because the H_2 line emission during the post-AGB phase makes the observed K-W3 colors bluer.

5.6. Discussion of $Fe_{0.9}Mg_{0.1}O$ and Alumina Dust

The SEDs of LMOA stars with thin dust shells suggest the presence of amorphous alumina (Al_2O_3) which is useful at $\lambda \sim 10$ μm (Suh 2016) and Fe-Mg oxides which is useful at $\lambda \sim 20$ μm (Th. Posch et al. 2002) as well as amorphous silicate dust.

Figure 7 shows opacity functions of warm silicate, alumina, and $Fe_{0.9}Mg_{0.1}O$ which are used for modelling LMOA stars with thin dust shells (see Section 4.1).

Suh & Kwon (2011) found that alumina dust is useful to fit the AKARI [9]-[12] colors. Because the emission feature of alumina at 11.8 μm influence the shape of the SED enhancing the emission at $\lambda \sim 12$ μm (see Figure 7), alumina dust would produce larger [9]-[12] colors. For LMOA stars, Suh (2016) found that the amorphous alumina dust (about 10-40%) mixed with amorphous silicate can reproduce the observations better (especially at $\lambda \sim 10$ μm) by comparing the theoretical models with the observations.

Henning et al. (1995) presented the optical constants for $Fe_xMg_{1-x}O$ (x=0.4-1.0) dust. For spherical grains, the peak wavelengths of the opacity function for $Fe_{0.4}Mg_{0.6}O$, $Fe_{0.9}Mg_{0.1}O$, and FeO are 17.7, 19.6, and 19.9 μm, respectively.

By analyzing short wavelength spectrometer (SWS) data from Infrared Space Observatory (ISO), Th. Posch et al. (2001) and Heras & Hony (2005) detected a broad dust emission feature peaking at 19.5 μm from many LMOA stars with thin dust shells. They suggested that the emission is due to $Fe_{0.9}Mg_{0.1}O$ dust and a mixture of different $Fe_xMg_{1-x}O$ (x=0.4-1.0) may also be compatible with the observational data.

$Fe_{0.9}Mg_{0.1}O$ dust emission would influence both of the WISE W4 and IRAS [25] fluxes (see Figure 5). We have found that the effect on the IRAS [12]-[25] color is much smaller than the effect on the WISE W3-W4 color. We expect that this could be because the WISE W4 [22 μm] detector is more sensitive to the $Fe_{0.9}Mg_{0.1}O$ dust emission (at 19.6 μm) compared with the IRAS [25 μm] detector.

6. SUMMARY

For a large sample of evolved stars (5036 AGB stars, 660 post-AGB stars, and 2748 PNe) in our Galaxy, we have presented various IR 2CDs using the IRAS PSC, AKARI PSC, 2MASS, and WISE data.

The theoretical dust shell model tracks using dust opacity functions of silicate, $Fe_{0.9}Mg_{0.1}O$, alumina, and AMC dust can roughly explain the observed points of AGB stars, post-AGB stars, and PNe on various IR 2CDs. Some discrepancies between theory and observations could be mainly because the theoretical models used in this work did not consider gas-phase radiation processes. Also, the spherically symmetric dust shell models did not consider some dust species (e.g., PAH) and non-spherical geometry.

WISE data are useful in studying the evolution of AGB stars and PNe, especially for dim objects. Because the WISE data are available for much larger sample of dim objects, they can be helpful to investigate the evolution in more details.

For all of the observed colors ([12]-[25], [25]-[60],

W2-W3, W3-W4, K-W3, and [9]-[12]), we have found that the averaged color of AGB stars is bluer than that of PNe. Note that this difference is systematic except for the K-W3 color, for which the error bars overlap. The main reason for this difference would be that detached dust shells generally produce redder colors during the post-AGB phase.

If MPNe are really older PNe, they would show some systematic color changes from normal PNe. We could not find any systematic color differences except for the IRAS [12]-[25] color, which shows bluer colors for MPNe.

$Fe_{0.9}Mg_{0.1}O$ dust is useful to fit the observed W3-W4 colors for O-rich AGB stars with thin dust shells. This could be because the WISE W4 band (22 μm) is more sensitive to the broad $Fe_{0.9}Mg_{0.1}O$ dust emission feature at $\lambda \sim 20$ μm than the IRAS [25] band.

ACKNOWLEDGMENTS

I thank the anonymous referees for constructive comments and suggestions. This work was supported by the National Research Foundation of Korea (NRF) grant funded by the Korea government (MSIT; Ministry of Science and ICT) (No. NRF-2017R1A2B4002328). This research has made use of the VizieR catalogue access tool, CDS, Strasbourg, France. This research has made use of the NASA/ IPAC Infrared Science Archive, which is operated by the Jet Propulsion Laboratory, California Institute of Technology, under contract with the National Aeronautics and Space Administration.

REFERENCES

Begemann, B., Dorschner, J., Henning, T., et al. 1997, Aluminum Oxide and the Opacity of Oxygen-Rich Circumstellar Dust in the 12-17 Micron Range, ApJ, 476, 199

Beichman, C. A., Neugebauer, G., Habing H., Clegg, P. E., & Chester, T. C. 1988, IRAS Catalogs and Atlases: Explanatory Supplement, NASA RP-1190 (Washington: NASA)

Cutri, R. M., Skrutskie, M. F., Van Dyk, S., et al. 2003, VizieR Online Data Catalog: 2MASS All-Sky Catalog of Point Sources

Davis, C. J., Smith, M. D., Stern, L., Kerr, T. H., & Chiar, J. E. 2003, Near-Infrared Spectroscopy of (Proto)-Planetary Nebulae: Molecular Hydrogen Excitation as an Evolutionary Tracer, MNRAS, 344, 262

Froebrich, D., Davis, C. J., Ioannidis, G., et al. 2011, UWISH2 – the UKIRT Widefield Infrared Survey for H_2, MNRAS, 413, 480

Gutenkunst, S., Bernard-Salas, J., Pottasch, S. R., Sloan, G. C., & Houck, J. R. 2008, Chemical Abundances and Dust in Planetary Nebulae in the Galactic Bulge, ApJ, 680, 1206

Henning, T., Begemann, B., Mutschke, H., & Dorschner, J. 1995, Optical Properties Of Oxide Dust Grains, A&AS, 112, 143

Heras, A. M., & Hony, S. 2005, Oxygen-Rich AGB Stars with Optically Thin Dust Envelopes, A&A, 439, 171

Hrivnak, B. J., Kwok, S., & Volk, K. M. 1989, A Study Of Several F And G Supergiant-Like Stars With Infrared Excesses As Candidates For Proto-Planetary Nebulae, ApJ, 346, 265

Ishihara, D., Acke, B., Verhoelst, T., et al. 2010, The AKARI/IRC Mid-Infrared All-Sky Survey, A&A, 514, A1

Ivezić, A., & Elitzur, M. 1997, Self-Similarity and Scaling Behaviour of Infrared Emission from Radiatively Heated Dust - I. Theory, MNRAS, 287, 799

Kerber, F., Mignani, R., Guglielmetti, F., & Wicenec, A. 2003, Galactic Planetary Nebulae and Their Central Stars I. An Accurate and Homogeneous Set of Coordinates, A&A, 408, 1029

Kohoutek, L. 2001, Version 2000 of the Catalogue of Galactic Planetary Nebulae, A&A, 378, 843

Kwok, S. 2000, The Origin and Evolution of Planetary Nebulae (Cambridge: Cambridge University Press)

Miszalski, B., Parker, Q. A., Acker, A., et al. 2008, MASH-II: More Planetary Nebulae from the AAO/UKST Hα Survey, MNRAS, 384, 525

Murakami, H., Baba, H., Barthel, P., et al. 2007, The Infrared Astronomical Mission AKARI, PASJ, 59, 369

Parker, Q. A., Acker, A., Frew, D. J., et al. 2006, The Macquarie/AAO/Strasbourg Hα Planetary Nebula Catalogue: MASH, MNRAS, 373, 79

Sevenster, M. N. 2002, OH-Selected AGB and Post-AGB Objects. I. Infrared and Maser Properties, AJ, 123, 2788

Suh, K.-W. 1999, Optical Properties of the Silicate Dust Grains in the Envelopes around Asymptotic Giant Branch Stars, MNRAS, 304, 389

Suh, K.-W. 2000, Optical Properties of the Carbon Dust Grains in the Envelopes around Asymptotic Giant Branch Stars, MNRAS, 315, 740

Suh, K.-W. 2004, Pulsation Phase-Dependent Dust Shell Models for Oxygen-Rich Asymptotic Giant Branch Stars, ApJ, 615, 485

Suh, K.-W. 2014, Astrophysics of Dusty Stellar Winds from AGB Stars, JKAS, 47, 219

Suh, K.-W. 2015, Infrared Two-Color Diagrams for AGB Stars, Post-AGB Stars, and Planetary Nebulae, ApJ, 808, 165

Suh, K.-W. 2016, Optical Properties of Amorphous Alumina Dust in the Envelopes Around O-Rich AGB Stars, JKAS, 49, 127

Suh, K.-W., & Hong, J. 2017, A New Catalog of AGB Stars Based on Infrared Two-Color Diagrams, JKAS, 50, 131

Suh, K.-W., & Kwon, Y.-J. 2011, Infrared Two-Colour Diagrams for AGB Stars Using AKARI, MSX, IRAS and Near-Infrared Data, MNRAS, 417, 3047

Suh, K.-W., & Kwon, Y.-J. 2013, Water Ice in High Mass-Loss Rate OH/IR Stars, ApJ, 762, 113

Szczerba, R., Siódmiak, N., Stasińska, G., & Borkowski, J. 2007, An Evolutionary Catalogue of Galactic Post-AGB and Related Objects A&A, 469, 799

Th. Posch, F., Kerschbaum, H., Mutschke, J., et al. 2002, On the Origin of the 19.5 μm Feature, A&A, 393, L7

van der Veen, W. E. C. J., & Habing, H. J. 1988, The IRAS Two-Colour Diagram as a Tool for Studying Late Stages of Stellar Evolution, A&A, 194, 125

Wright, E. L., Eisenhardt, P. R. M., Mainzer, A. K., et al. 2010, The Wide-Field Infrared Survey Explorer (WISE): Mission Description And Initial On-Orbit Performance, AJ, 140, 1868

Yamamura, I., Makiuti, S., Ikeda, N., et al. 2010, AKARI/FIS All-Sky Survey Bright Source Catalogue Version 1.0 Release Note